1   **Revision 1**

2   **Revision of the CaCO$_3$–MgCO$_3$ phase diagram at 3 and 6 GPa**

3

4   Anton Shatskiy[1,2*], Ivan V. Podborodnikov[1,2], Anton V. Arefiev[1,2], Daniil A. Minin[1,2], Artem D.

5   Chanyshev[1,2], Konstantin D. Litasov[1,2]

6

7   [1]V.S. Sobolev Institute of Geology and Mineralogy, Russian Academy of Science, Siberian

8   Branch, Novosibirsk 630090, Russia

9   [2]Novosibirsk State University, Novosibirsk 630090, Russia

10   *telephone/fax: +7 (383)-330-75-01, e-mail: shatskiy@igm.nsc.ru

11

12   **Abstract**

13   Subsolidus and melting relationships for the system CaCO$_3$–MgCO$_3$ have been reexamined

14   using a Kawai-type multianvil apparatus at 3 and 6 GPa in graphite capsules. Phase boundaries were

15   delineated according to the chemical composition of phases measured by electron microprobe in

16   energy dispersive mode and identification of crystal phases by Raman spectroscopy.

17   At 3 GPa, the dolomite-magnesite solvus intersects the melting loop at about 1250 °C, and the

18   isothermal three-phase line so produced represents the peritectic reaction: dolomite (Ca# 43) =

19   magnesite (Ca# 13) + liquid (Ca# 48), where Ca# = 100·Ca/(Ca+Mg). The melting loop for the

20   CaCO$_3$–MgCO$_3$ join extends from 1515 °C (CaCO$_3$) to 1515 °C (MgCO$_3$) through a liquidus

21   minimum at 1230 °C (near 53 mol% CaCO$_3$). Starting from 1425 °C at ≤ 30 mol% CaCO$_3$ in the

22   system, the liquid quenches to dendritic carbonate and periclase and contains rounded voids,

23   indicating an incongruent melting reaction: MgCO$_3$ (magnesite) = MgO (in liquid) + CO$_2$ (fluid

24   and/or liquid).

25   At 6 GPa, aragonite + magnesite assemblage is stable up to 1000 °C. The reaction aragonite +

26   magnesite = dolomite locates between 1000 and 1050 °C. The presence of dolomite splits the system

27   into two partial binaries: aragonite + dolomite and dolomite + magnesite. The dolomite-magnesite

28   solvus intersects the melting loop between 1400 and 1450 °C, and the isothermal three-phase line so

29   produced represents the peritectic reaction: dolomite (Ca# 31) = magnesite (Ca# 21) + liquid (Ca#

30   57). The melting loop for the CaCO$_3$–MgCO$_3$ join extends from 1660 °C (CaCO$_3$) to 1780 °C

31   (MgCO$_3$) through a liquidus minimum at 1400 °C and 62 mol% CaCO$_3$.

32   The compositions of carbonate crystals and melts from the experiments in the carbonated

33   eclogite (Yaxley and Brey, 2004) and peridotite (Dalton and Presnall, 1998) systems are consistent

34   with the geometry of the $CaCO_3$-$MgCO_3$ melting loop at 3 and 6 GPa: Ca-dolomite melt coexists

35   with Mg-calcite in eclogite and peridotite at 3 GPa and dolomite melt coexists with magnesite in

36   peridotite at 6 GPa.

37   **Keywords:** $CaCO_3$-$MgCO_3$, phase relations, high-pressure, magnesite, dolomite, calcite,

38   aragonite, Earth's mantle

39

40   **Introduction**

41   The $(Ca,Mg)CO_3$ carbonates are the most important carbon-bearing phases entering

42   subduction zones and are believed to survive along most subduction P-T profiles through the island

43   arc magma generation depths (Kerrick and Connolly, 2001a; b). The evidence for the deep

44   subduction of carbonates arises from the findings of Ca-Mg carbonates associated with diamond in

45   CO_2-bearing inclusions within xenoliths from a forearc magmatic rock in southwest Japan

46   (Murakami et al., 2008). Another evidence originates from continental crust exhumed from mantle

47   depths. The recovered ultrahigh-pressure (UHP) metamorphic rocks contain coesite and diamond

48   with variable amounts of Ca-Mg carbonates as rock-forming minerals and/or as inclusions in high-

49   pressure minerals (Sobolev and Shatsky, 1990; Shatsky et al., 1995; Dobrzhinetskaya et al., 2006;

50   Korsakov and Hermann, 2006; Korsakov et al., 2009). Presence of Ca-Mg-carbonates at different

51   levels of lithospheric mantle is apparent through the occurrence of calcite (Cal), dolomite (Dol), and

52   magnesite (Mgs) in spinel peridotite xenoliths (Amundsen, 1987; Ionov et al., 1993; Kogarko et al.,

53   1995; Ionov et al., 1996) and as inclusions in kimberlitic diamonds (Meyer and McCallum, 1986;

54   Bulanova and Pavlova, 1987; Phillips and Harris, 1995; Wang et al., 1996; Sobolev et al., 1997;

55   Stachel et al., 1998; Shatsky et al., 2008; Zedgenizov et al., 2014).

56   High-pressure experiments revealed that Ca-Mg carbonates become stable at the solidus of

57   carbonated peridotites, eclogites, and pelites at depths greater than 70–90 km (Wyllie and Huang,

58   1975; Eggler, 1978; Wallace and Green, 1988; Dalton and Presnall, 1998; Dasgupta et al., 2004;

59   Yaxley and Brey, 2004; Dasgupta and Hirschmann, 2007; Thomsen and Schmidt, 2008; Litasov and

60   Ohtani, 2009; Litasov and Ohtani, 2010; Grassi and Schmidt, 2011; Kiseeva et al., 2013; Thomson

61   et al., 2016). Once carbonate becomes stable in the subsolidus, it plays a major role in the melting

62   reaction, yielding essentially dolomitic liquid. Thus, phase relations in the $CaCO_3$–$MgCO_3$ system

63   are important for understanding possible storage of carbonates in subduction process, as well as

2

64   genesis of essentially carbonated magmas such as carbonatites and kimberlites in the mantle (Wyllie

65   and Huang, 1975).

66   Irving and Wyllie (1975) have studied subsolidus and melting phase relations along the join

67    $CaCO_3$–$MgCO_3$ at 3.0 GPa (2.7 GPa after pressure correction reported by Byrnes and Wyllie

68   (1981)) using a piston-cylinder apparatus (Fig. 1a). In spite of high accuracy of pressure (± 0.07

69   GPa) and temperature measurements (± 13°), the technical limitations of analytical methods

70   available at that time produce some ambiguities. Namely, the powder X-ray diffraction is not a

71   reliable guide to determine the melting phase relations, because it is useless for determination of

72   chemical composition of quenched melt and yields large uncertainty in compositions of supersolidus

73   carbonates as can be seen in Fig. 1a. Buob (2003) and Buob et al. (2006) studied the $CaCO_3$–

74    $MgCO_3$ join at 6 GPa employing a Walker-type multi-anvil module. Yet, this study mainly focused

75   on the subsolidus phase relationships, leaving largely unconstrained the melting relationships (Fig.

76   1b).

77   Thus, the generally accepted $CaCO_3$–$MgCO_3$ phase diagrams at 3 and 6 GPa (Fig. 1) have

78   significant uncertainties for the solvus and liquidus. In view of the future research into more

79   complex alkali-bearing carbonate and carbonate-silicate systems, we decided that the uncertainties

80   in the $CaCO_3$–$MgCO_3$ diagrams would first be eliminated.

81

82   **Experimental procedure**

83   Experiments were performed in a uniaxial 1500-ton press, 'Discoverer', equipped with DIA-

84   type guide bock installed at the V.S. Sobolev Institute of Geology and Mineralogy SB RAS in

85   Novosibirsk, Russia (IGM SB RAS). "Fujilloy N-05" 26-mm tungsten carbide cubes with truncation

86   edge length of 12 mm were employed as Kawai-cell anvils. Pressure media shaped as 20.5 mm

87   octahedra without edges and corners were ground from semi-sintered ZrO_2 ceramics (OZ-8C,

88   MinoYogyo Co., Ltd). Pyrophyllite gaskets, 4.0 mm in both width and thickness were used to seal

89   the compressed volume and support the anvil flanks.

90   The design of the cell assembly is shown in Fig. 2. The cell contains several samples, 1 mm in

91   diameter and length, loaded into graphite holders (cassettes) with a 3.5 mm outer diameter,

92   surrounded by electrically insulating sleeves made of talc dehydrated at 1000 °C for 1 h and ZrO_2

93   plugs inserted at both heater ends. The high temperature was generated using a graphite heater,

94   4.5/4.0 mm in outer/inner diameter and 11 mm in length. The sample temperature was monitored via

95   a $WRe_{3\%}$-$WRe_{25\%}$ thermocouple, 0.1 mm in diameter, inserted through the heater walls and

3

96   electrically insulated by Al_2O_3 tubes. Thicker (0.3 mm) thermocouple extensions were inserted from

97   the exterior, through gasket holes, into the pressure medium to the point where the Al_2O_3 tubes

98   begin. No correction for the effect of pressure on the thermocouple electromotive force was applied.

99   The temperature gradient across the sample charges was examined, using thermal modeling software

100 (Hernlund et al., 2006), and was found to be about 5 and 7 °C/mm at 1000 and 1800 °C, respectively

101 (Shatskiy et al., 2011).

102   Room-temperature pressure calibration was performed by monitoring the resistance changes in

103 Bi at 2.5 and 7.7 GPa (Decker et al., 1972) using the same technique as in Shatskiy et al. (2011).

104 High-temperature pressure calibration was carried out using known phase transitions in SiO_2

105 (quartz-coesite) at 850–900 °C (Hemingway et al., 1998) and in $CaGeO_3$ (garnet-perovskite) at 950–

106 1000 °C (Ono et al., 2011) (Fig. 3). The pressure deviation from desirable values, during heating to

107 1900 °C, in the cell and press load did not exceed ±0.5 GPa. This was confirmed by *in situ* X-ray

108 diffraction experiments at the BL04B1 beamline of the 'SPring-8' synchrotron radiation facility

109 (Shatskiy et al., 2013).

110   Starting materials for the experimental study were analytical grade $CaCO_3$ and natural

111 $Mg_{0.975}Fe_{0.015}Mn_{0.006}Ca_{0.004}CO_3$ magnesite from Brumado (Bahia, Brazil). Requisite molar

112 proportions of these phases were thoroughly mixed and ground with agate mortar and pestle under

113 acetone. The prepared mixtures were loaded as a powder into graphite cassettes. The loaded

114 cassettes were dried at 300 °C for 1–2 h. Prepared assemblies were stored at 200 °C in a vacuum

115 oven for ≥12 h prior to experiment. The bulk compositions of the starting materials were verified

116 using the energy-dispersive X-ray (EDS) spectra, which were collected by rastering an electron

117 beam over a surface area of post-experimental samples with homogeneous textures obtained below

118 the solidus and above the liquidus (Tables 1-2).

119   The experiments were performed by compression to desirable load (3.0 or 6.5 MN) at a rate of

120 1 MN/h and then heating to a target temperature at a rate of 40-50 °C/min. The temperature was

121 maintained within 2.0 °C of the desired value, using a temperature control mode at a constant press

122 load. The experiments were terminated by turning off the power, resulting in a temperature drop to

123 <100 °C in 10–20 s, followed by slow decompression at a rate of 0.7–1.0 MN/h.

124   Recovered samples were mounted into epoxy and polished using the procedure described by

125 (Shatskiy et al., 2017). Samples were studied using a MIRA 3 LMU scanning electron microscope

126 (Tescan Orsay Holding) coupled with an INCA energy-dispersive X-ray microanalysis system 450

127 equipped with the liquid nitrogen-free Large area EDS X-Max-80 Silicon Drift Detector (Oxford

4

128   Instruments Nanoanalysis Ltd) at IGM SB RAS. The EDS spectra were collected by using an

129   electron beam-rastering method, in which the stage is stationary while the electron beam moves over

130   the surface area, with dimensions 5–10 μm (for mineral phases) and 50–500 μm (for a quenched

131   melt) at 20 kV accelerating voltage and 1.5 nA beam current. Live counting time for X-ray spectra

132   was 30 s (Lavrent'ev et al., 2015).

133   The Raman measurements were performed using a Horiba Jobin Yvon LabRAM HR800

134   Raman microspectrometer with the 514 nm line of an Ar-ion laser at IGM SB RAS (Shatskiy et al.,

135   2015).

136

137   **Experimental results**

138   The results of the experiments are summarized in Supplemental Tables 1 and 2. Positions of

139   phase boundaries were verified according to the phase composition of recovered samples and

140   chemical composition of phases measured by electron microprobe in the EDS mode. The crystal

141   phases, aragonite and calcite, were identified by Raman spectroscopy.

142

143   ***Experiments at 3 GPa***

144   Representative backscattered electron (BSE) images of samples recovered from 3 GPa

145   experiments are shown in Fig. 4. Fig. 5 shows the starting compositions, temperatures of runs and

146   phase compositions, as well as phase boundaries based on interpretation of these runs.

147   At 1000–1200 °C, the samples are represented by a single-phase aggregate of the calcite-

148   dolomite solid solution on the Ca-rich side (Figs. 4a, 4c, and 5) and by two phase region of Dol +

149   Mgs on the Mg-rich side (Figs. 4b, 4d, and 5). The dolomite-magnesite miscibility gap narrows from

150   Dol(50)–Mgs(6) to Dol(43)–Mgs(11) as temperature increases from 1000 to 1200 °C (Supplemental

151   Table 1, Fig. 5). The numbers in brackets indicate Ca# of corresponding phases.

152   The melting was established at 1250 °C and X(Ca) = 20–70 mol% (Supplemental Table 1, Fig.

153   5). The quenched liquid (L) forms a dendritic aggregate of carbonate crystals in the hot (HT) zone of

154   the charge (Figs. 4e-4g). At X(Ca) = 70 mol%, the sample consists of melt pool, L(57), in the hot

155   zone, the Cal(78) layer in the central zone and Dol(67) at the low-temperature (LT) side (Fig. 4e).

156   The dolomite composition is close to the sample bulk composition and, therefore, represents

157   subsolidus phase, whereas Cal(78) + L(57) represent supersolidus assemblage. At X(Ca) = 57 mol%,

158   compositions of liquid, L(55), and solid, Dol(58), are similar to the sample bulk composition (Fig.

159   4f). Simultaneous appearance of subsolidus and supersolidus phases can be connected with thermal

5

160   gradient and slight deviation of the system from ideal binary owing presence of additional

161   component, namely carbon from graphite capsules. The same situation was observed at $X(Ca) = 50$

162   mol%, where L(49) appears in coexistence with Dol(48) (Supplemental Table 1). The Mgs(13) +

163   Dol(42) + L(~50) assemblage was established at $X(Ca) = 30$ and 40 mol% (Fig. 4g) indicating a

164   peritectic reaction at 1250 °C (Fig. 5):

165    $$\text{Dol(42)} \rightarrow \text{Mgs(13)} + \text{L(50)}. \tag{1}$$
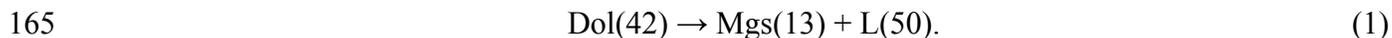
166   Our results suggests that the $CaCO_3$-$MgCO_3$ liquidus minimum locates between 48 and 55 mol%

167    $CaCO_3$ and between 1200 and 1250 °C, i.e., near 53 mol% $CaCO_3$ and 1225 °C (Fig. 5).

168   At 1300 °C, Cal(83) coexists with L(63) on the Ca-rich side (Fig. 4h), while Mgs(~89)

169   coexists with L(~45) on the Mg-rich side (Figs. 4j and 5). At $X(Ca) = 50$ mol%, the sample was

170   completely molten (Fig. 4i). With further temperature increase, Ca# of Mg-calcite and coexisting

171   liquid increases, whereas Ca# of magnesite and coexisting liquid decreases, so that a single phase

172   field of liquid expands (Fig. 5).

173   At 1430–1550 °C and $X(Ca) \leq 30$ mol%, the quenched melt and magnesite crystals contain

174   rounded voids, 50–200 μm in diameter (Figs. 4l-4q), and MgO in form of tiny worms within the

175   dendrite aggregate (Figs. 4q and 4r). This suggests incongruent melting reaction for dolomite-

176   magnesite solid solution (Ca-Mgs) and for pure magnesite:

177    $$\text{MgCO}_3 \text{ (Mgs or Ca-Mgs)} \rightarrow \text{MgCO}_3 \text{ (L)} + \text{MgO (L)} + \text{CO}_2 \text{ (Fluid)}. \tag{2}$$
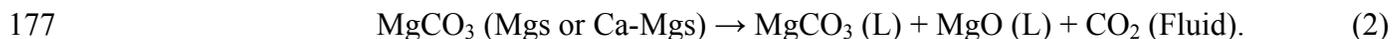
178   Unlike magnesite, calcite and calcite-dolomite solid solution melt congruently (Figs. 4k and 4o).

179   The melting temperatures of pure end-members, $CaCO_3$ and $MgCO_3$, were determined by the

180   falling-sphere technique (Fig. 4o). In addition, the textural criteria were used for identification of

181   magnesite incongruent melting (Figs. 4q and 4r). We found that both carbonates remain solid up to

182   1500 °C (Fig. 4m) and melts at 1525 °C (Figs. 4p and 4o).

183

184   ***Experiments at 6 GPa***

185   The textures of samples recovered from subsolidus and supersolidus runs are illustrated in Fig.

186   6. At 900 and 1000 °C, aragonite and magnesite of near end-member composition coexist

187   (Supplemental Table 2, Fig. 7). At 1050 °C, the presence of dolomite splits the system into two

188   partial binaries (Fig. 7). Arg(100) and Dol(58) coexist on the Ca-rich side (Figs. 6a and 6b), while

189   Dol(49) and Mgs(6) appear on the Mg-rich side (Figs. 6c and 6d). As temperature increases, the two

190   phase field on the Ca-rich side narrows asymmetrically owing increasing Ca# of rhombohedral

191   carbonate to 80-84 and 98 mol% at 1050 and 1300 °C, respectively (Figs. 6d-6f, and 7). On the Mg-

192 rich side the miscibility gap narrows to Dol(34)–Mgs(18) as temperature increases to 1400 °C (Figs.

193 6i and 7).

194 The first melt of eutectic composition, L(62), was established in coexistence with Dol(59) at

195 1400 °C and X(Ca) = 60 mol% (Figs. 6g, 6h, and 7). At 1450 °C and X(Ca) = 70–80 mol%, L(67–

196 73) coexists with Cal(77–83) (Figs. 6j, 6k, and 7), while at X(Ca) = 20–50 mol%, L(56-59) coexists

197 with Mgs(14–18) (Figs. 6l, 6m, and 7). In addition to Mgs, the LT zone contains subsolidus

198 dolomite (Figs. 6l and 6m). The dolomite composition is close to the sample bulk composition

199 (Supplemental Table 2). Our results indicate that the dolomite-magnesite solvus intersects the

200 $CaCO_3$-$MgCO_3$ melting loop between 1400 and 1450 °C to produce a peritectic reaction (Fig. 7):

201 $$Dol(31) \rightarrow Mgs(21) + L(57). \tag{3}$$
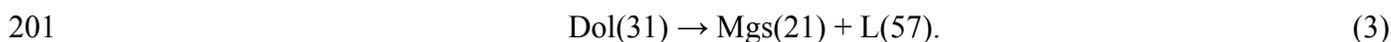
202 With further temperature increase, Ca# of Mg-calcite and coexisting liquid increases, while

203 Ca# of magnesite and coexisting liquid decreases (Fig. 7). At 1600 °C, Cal(95) coexists with L(90)

204 (Fig. 6n). At 1800 °C, Mgs(2) appears in coexistence with L(14) (Fig. 6s). Based on the falling-

205 sphere experiments, $CaCO_3$ remains solid up to 1650 °C and melts at 1700 °C (Figs. 6q and 6r).

206 Magnesite melts incongruently between 1750 and 1800 °C to produce MgO-bearing $MgCO_3$ melt

207 and CO_2 fluid (Figs. 6t and 6u).

208

209 **Discussion**

210 The general geometry of the phase diagram at 3 and 6 GPa is consistent with that deduced for

211 2.7 GPa by Irving and Wyllie (1975) and for 6.0 GPa by Buob et al. (2006) (Fig. 8). At 3 GPa, the

212 dolomite-magnesite solvus replicates that determined by Irving and Wyllie (1975) (Fig. 8a). At 6

213 GPa, the dolomite-magnesite solvus and the aragonite + dolomite two phase field were found to be

214 in agreement with those reported by Buob et al. (2006) within experimental error (Fig. 8b).

215 The obtained melting phase relations, however, exhibit significant inconsistencies. Although,

216 the shape of 3 GPa melting loop is very close to that determined by Irving and Wyllie (1975), it is

217 shifted by 65-135 °C to the lower temperatures (Fig. 8a). To check the possible temperature

218 underestimation in our experiments, we used a gold marker. We found that at a pressure of 3 GPa,

219 Au remains solid at 1175 °C and melts at 1250 °C. If the uncertainty is caused by the temperature

220 underestimation, our 1175 °C should correspond to 1240-1310 °C, i.e. exceeds the Au melting

221 temperature, T_{Au} = 1235 °C at 3 GPa (Akella and Kennedy, 1971)), which disagrees with our

222 observations. Thus, there should be another reason for the discrepancy.

7

223   Alternatively, a pressure underestimation can lower the temperatures of solidus and liquidus.

224   Based on the $CaCO_3$ melting curve (Irving and Wyllie, 1975), the established melting temperature

225   of calcite, 1515 °C, corresponds to 1.6 GPa (Fig. 9). Under this pressure, magnesite must dissociate

226   to periclase (Per) and CO_2 fluid at 1300 °C (Fig. 10) (Irving and Wyllie, 1975). However, in our 3

227   GPa experiments, magnesite remains stable up to 1500 °C and melts incongruently at 1525 °C to

228   produce liquid and CO_2 fluid (Fig. 5) like in the study by Irving and Wyllie (1975) at 2.75 GPa and

229   1600 °C. According to their experiments, the magnesite dissociation occurs at pressures of ≤ 2.5

230   GPa (Fig. 10b). At these pressures, the dissociation of magnesite and dolomite solid solutions

231   produces extensive fields including periclase and CO_2 fluid (Irving and Wyllie, 1975; Byrnes and

232   Wyllie, 1981) (Fig. 11a). Thus, the observed incongruent melting of magnesite and dolomite solid

233   solutions (Fig. 5) suggests that the pressure underestimation if any in our 3 GPa experiments cannot

234   exceed 0.5 GPa, and therefore, cannot account the discrepancy in the solidus and liquidus

235   temperatures in our and Irving and Wyllie (1975) studies (Fig. 8a).

236   In Irving and Wyllie (1975) study, the run durations were limited to a few minutes in most

237   experiments to minimize contamination of Pt-PtRh$_{10\%}$ thermocouple and access of water from the

238   talc-bearing pressure-transmitting medium. Unlike we used WRe$_{3\%}$-WRe$_{25\%}$ thermocouple and

239   anhydrous ceramics for the cell assembly (Fig. 2). This allowed conducting long duration

240   experiments without taking care about drift of thermocouple EMF and sample contamination by

241   water (Supplemental Tables 1 and 2). It is well known that the melting reaction can be delayed to

242   higher temperatures if the rate of heating is fast and run duration is too short (Haines, 2002). That

243   would be the reason of the higher temperatures of the $CaCO_3$-$MgCO_3$ melting loop determined by

244   Irving and Wyllie (1975). Yet, $CaCO_3$ melting in run no. D076 with duration of 5 min at 1525 °C

245   and 3 GPa (Supplemental Tables 1) contradicts to this suggestion, since the 1595–1620 °C, 2.7 GPa

246   bracket for $CaCO_3$ melting in Huang and Wyllie (1976) study was established in the runs with the

247   same duration. Their results duplicate the bracket established by Irving and Wyllie (1975) in 2 min

248   runs and elliminates any doubt on the effect of thermocouple types, because Huang and Wyllie

249   (1976) employed WRe$_{5\%}$-WRe$_{26\%}$ thermocouple.

250   The presence of additional components can also shift the melting loop to lower temperature. In

251   both our and Irving and Wyllie (1975) studies, all starting mixtures were carefully dried. Thus, a

252   fluxing effect of water can be excluded. On the other hand, the capsule material is also an additional

253   component (graphite in our study and Pt in Irving and Wyllie study). Both C and Pt are soluble in

254   carbonate melts and apparently have a eutectic relationship with carbonates. Consequently, C and Pt

8

255 can lower apparent solidus and liquidus temperatures in carbonate systems. The discrepancy,

256 therefore, could be attributed to higher fluxing effect of C than Pt. Yet, the lower solidus and

257 liquidus temperatures established by Buob et al. (2006) for the $CaCO_3$-$MgCO_3$ join using Pt

258 capsules as well as the results of falling-sphere experiments of Li et al. (2017) on $CaCO_3$ melting in

259 Pt capsules is inconsistent with this idea (Figs. 8b and 9). Thus, we finally conclude that the

260 difference in temperatures of the $CaCO_3$-$MgCO_3$ melting loop can be connected with short duration

261 of experiments in Irving and Wyllie (1975) study.

262   The eutectic and peritectic compositions and consequent liquidus lines were found to be

263 consistent within 5 mol% with those reported by Irving and Wyllie (1975) (Fig. 8a). The minor

264 deviation would be attributed to the technical limitations of analytical methods available at that time.

265 The compositions of rhombohedral Ca-Mg carbonates in Irving and Wyllie (1975) study were

266 estimated from a curve calibrated using the position of the 2θ of [104] peak determined by powder

267 X-ray diffraction patterns . This method is reliable to determine subsolidus relationships if

268 equilibrium has been achieved. Yet, this technique is of little use for supersolidus samples, because

269 carbonate melt quenches to an aggregate of carbonate crystals, which differs in composition from

270 the melt. Furthermore, the X-ray diffraction peaks of carbonates crystallized from the melt during

271 quenching could complicate selection of peaks of carbonates formed under stationary conditions.

272   Buob (2003) and Buob et al. (2006) studied the $CaCO_3$–$MgCO_3$ join at 6 GPa. Their main

273 interest was to determine the subsolidus phase relationships, but some supersolidus experiments

274 were also conducted. However, the supersolidus data are too scattered to constrain melting phase

275 relationships (Fig. 1b). The 6 GPa liquidus minimum at 1400 °C and Ca# (62) established in our

276 study has distinctly higher Ca# compared with that postulated by Buob et al. (2006) at 1350 °C and

277 Ca# (~50) (Fig. 8b). Their proposal is based on the results of two runs with $X(Ca)$ = 50 mol%: at

278 1350 °C, where dolomite is solid, and at 1400 °C, where dolomite completely melts (Fig. 1b).

279 Obviously, these data are not enough to determine the eutectic melt composition. Furthermore, these

280 data suggest that liquidus minimum is located at higher temperature than the peritectic (Fig. 1b). The

281 peritectic point established near 1440 °C and Ca# (57) in our study also differs from that in Buob et

282 al. (2006) study, 1350 °C and Ca# (39) (Fig. 8b). Buob et al. (2006) comment on the ambiguities in

283 the interpretation of the melting relationships because of problem in distinguishing quench and

284 stable crystals, which do not show clear grain boundaries. Besides, the large spread of melt

285 composition data points would be caused by applying the stationary electron beam in wavelength

286 dispersive mode, which diameter (up to 10 μm) is comparable with quenched melt grain size.

9

287   Calcite melts incongruently at pressures below the singular point, which is located between

288   0.1 and 0.7 GPa, according to the reaction: Cal = L + F (Irving and Wyllie, 1975). At higher

289   pressures, it melts congruently as shown in Fig. 9. The melting point of $CaCO_3$ determined in the

290   present study by the falling-sphere technique rises from 1515 at 3 GPa to 1780 °C at 6 GPa (Fig. 9).

291   These results are in reasonable agreement with the melting temperatures established using the same

292   technique in Li et al. (2017) study, but lower by about 80 °C than those measured by monitoring

293   resistance change during sample heating (Li et al., 2017) and by about 90 °C than those established

294   in quench experiments using textural criteria for melt identification (Irving and Wyllie, 1975) (Fig.

295   9).

296   Magnesite dissociates to periclase (Per) and CO_2 fluid at pressures below the invariant point Q

297   located near 2.6 GPa (Fig. 10) (Irving and Wyllie, 1975). At 3 GPa and 1515 °C, magnesite melts

298   incongruently according to the reaction 2 (Fig. 10). Although, the incongruent melting of magnesite

299   in Irving and Wyllie (1975) study occurs at slightly lower pressure, 2.75 GPa, and higher

300   temperature, 1610 °C (Fig. 10), the melting reaction is the same: Mgs = L + F. At the same time it

301   differs from that proposed by Huang and Wyllie (1976), Mgs = L + Per. Above the singular point S,

302   magnesite melts congruently (Fig. 10). Our 6 GPa melting point is consistent with the existing data

303   on magnesite congruent melting at 3.6 GPa (Irving and Wyllie, 1975), 8 and 15 GPa (Katsura and

304   Ito, 1990) (Fig. 10).

305   Our 3 GPa data, combined with previous works at the lower pressures (Irving and Wyllie,

306   1975; Byrnes and Wyllie, 1981), document a shift in the eutectic melt composition in the $CaCO_3$–

307    $MgCO_3$ system to more magnesian compositions with increasing pressure, from Ca# (89) at 0.5

308   GPa, Ca# (67) at 1 GPa, to Ca# (53) at 3 GPa (Figs. 11a and 11b). However, our 6 GPa experiments

309   with the minimum melt at Ca# of 62 indicate that this tendency is not maintained as pressure

310   increases to 6 GPa (Fig. 11c).

311

312   **Implication**

313   It was suggested that the composition of the first liquid produced at the solidus of carbonated

314   peridotite and eclogite at high pressure is strongly influenced by the melting phase relations in the

315    $CaCO_3$–$MgCO_3$ system (Wyllie and Huang, 1976; Eggler, 1978; Dalton and Presnall, 1998; Yaxley

316   and Brey, 2004; Luth, 2006; Dasgupta and Hirschmann, 2007). It is, therefore, important to compare

317   our results in the silicate-absent system with those in the CaO–MgO–Al_2O_3–SiO_2–CO_2 (CMAS-

10

318   CO_2) (Dalton and Presnall, 1998) and even Na-poor carbonated eclogite systems (Yaxley and Brey,

319   2004).

320   Dalton and Presnall (1998) experimentally determined the phase relationships in the CMAS-

321   CO_2 system from 3 to 7 GPa. At 3 GPa, the first liquid produced by melting of assemblage of

322   forsterite, enstatite, diopside and dolomite has Ca# (59) and coexists with Dol (68). This is

323   consistent with phase relations established at the Ca-rich side of the $CaCO_3$–$MgCO_3$ binary (Fig.

324   12a). At 4.8 GPa and 1320 °C, the solidus carbonate changes from dolomite to magnesite (Dalton

325   and Presnall, 1998). Owing to this transition the melting has to be controlled by the Mg-rich side of

326   the $CaCO_3$–$MgCO_3$ binary. Indeed, an appearance of Mgs (7) in coexistence with L (49) at the

327   CMAS-CO_2 solidus at 6 GPa is consistent with the melting relationships at the Mg-rich side of the

328    $CaCO_3$–$MgCO_3$ binary (Fig. 12b). However, based on our results this assemblage should appear at

329   150 °C higher temperature (Fig. 12b). On the other hand, the 6 GPa results reported by Luth (2006)

330   for the $CaCO_3$+MgO+$2SiO_2$ system, Keshav et al. (2005) for the CMAS-CO_2 system, and Shatskiy

331   et al. (2017) for the $CaMgSi_2O_6$+$2MgCO_3$ system are consistent within 50 °C with phase

332   relationships established at the Mg-rich side of the $CaCO_3$–$MgCO_3$ binary (Fig. 12b). The Ca# of

333   carbonate, Cal(82), and coexisting melt, L(60), of Yaxley and Brey (2004) obtained from a

334   carbonated eclogite at 3 GPa is again consistent with the Ca-rich side of the $CaCO_3$–$MgCO_3$ binary.

335   The Cal(82) + L(60) assembly, however, appears at 90 °C lower temperature relative to the $CaCO_3$–

336    $MgCO_3$ data (Fig. 12a). Despite the temperature differences, the close match of liquid and solid

337   carbonate compositions indicates that the incipient melting in SiO_2-bearing carbonated systems at 3

338   and 6 GPa closely approach pure carbonate melting (Fig. 12).

339

340   **Acknowledgements**

345

346
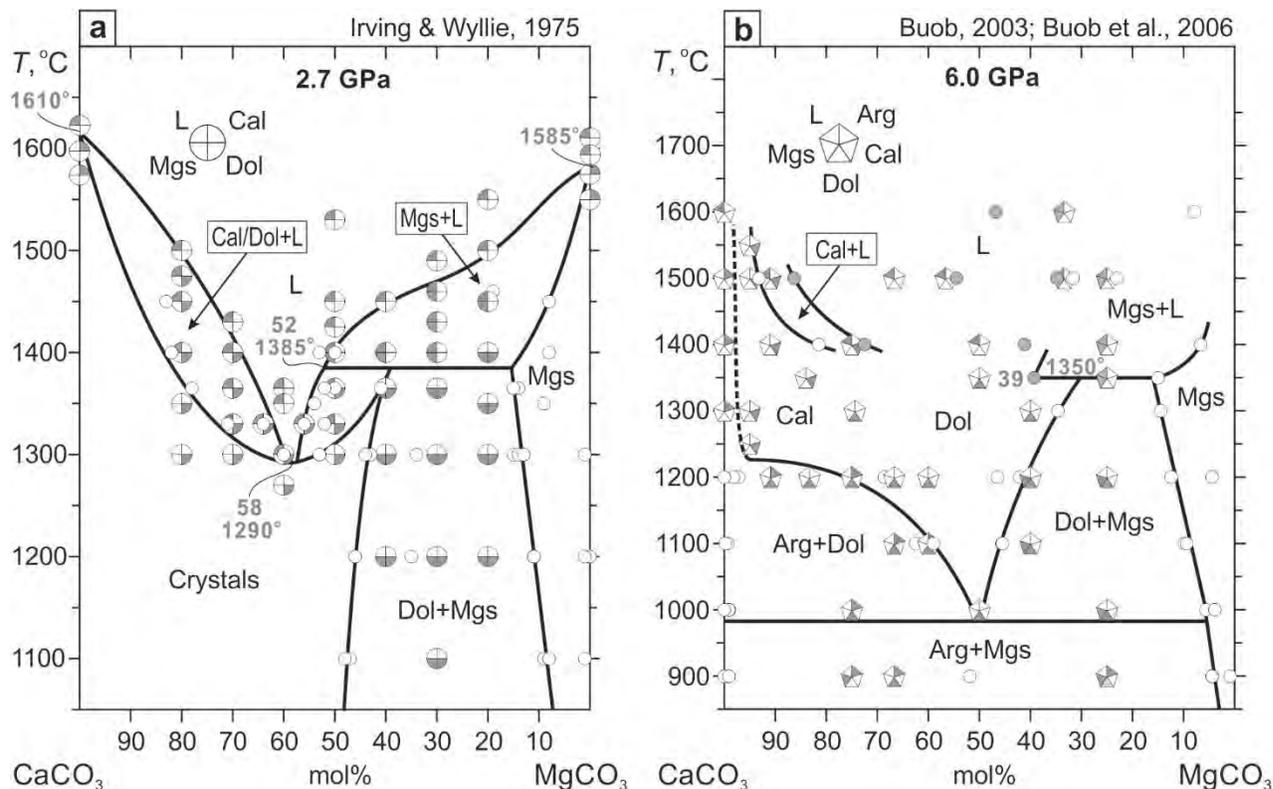
Fig. 1. Previous experimental data on phase relations for the system $CaCO_3$-$MgCO_3$ at 3.0 GPa modified after Irving and Wyllie (1975), with pressure correction as reported by Byrnes and Wyllie (1981) (a), and at 6.0 after Buob (2003), and Buob et al. (2006) (b). Arg – aragonite, Cal and Mg-Cal – pure and Mg-bearing calcite, Dol – dolomite, Mgs – magnesite, L – liquid. Open and grey circles indicate composition of solid and liquid phases. The compositions of solid phases obtained at 3 GPa were determined from 2θ values of [104] X-ray diffraction peaks (Irving and Wyllie, 1975) (a). Composition of phases recovered from 6 GPa experiments were determined by electron microprobe (Buob, 2003; Buob et al., 2006) (b). Grey numbers indicate composition (mol% $CaCO_3$) and temperature (°C) of eutectic and peritectic points.
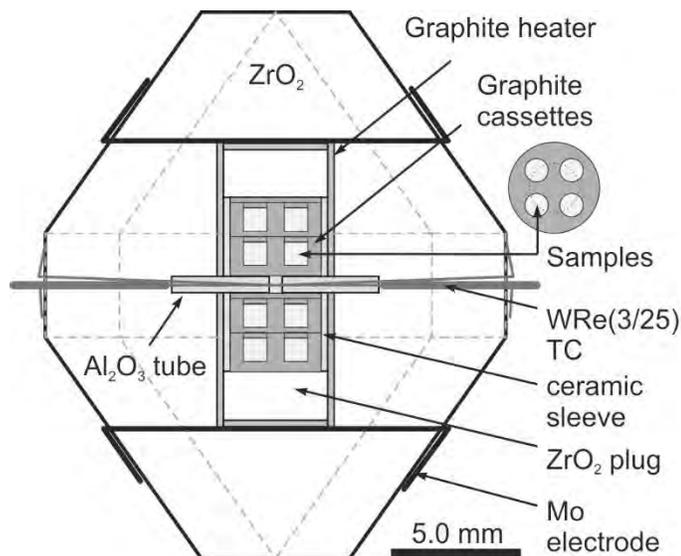
Fig. 2. High-pressure cell assembly employed to study phase relations in the $CaCO_3$-$MgCO_3$ system at 3 and 6 GPa using a uniaxial press Kawai-type press with DIA guide block. TC – thermocouple.
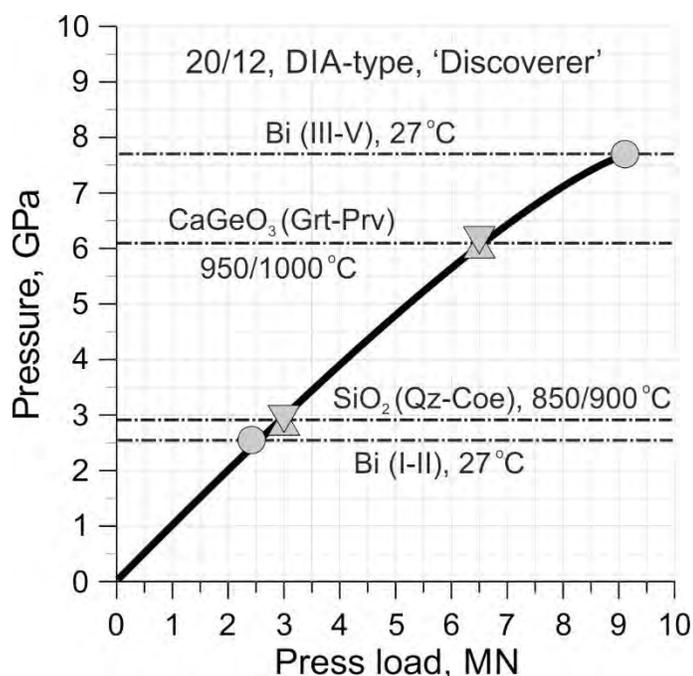
Fig. 3. Pressure calibration for the ZrO_2 high-pressure cell (pressure medium edge length 20.5 mm, truncation edge length of WC anvils is 12.0 mm, and pyrophyllite gaskets, 4.0 mm in width and thickness) compressed by the DIA-type uniaxial press. Qz – quartz, Coe – coesite, Grt – garnet, Prv – perovskite.

Run No.; $X(CaCO_3)$, mol%; temperature; run duration

a. D084; 80; 1000 °C; 4 h.
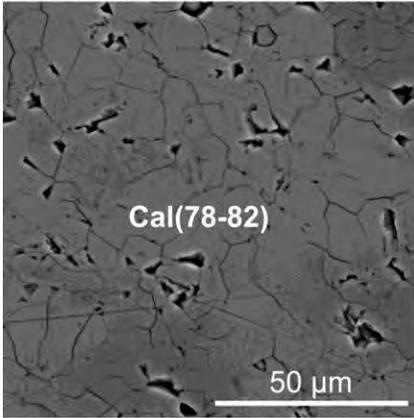
b. D084; 40; 1000 °C; 4 h.
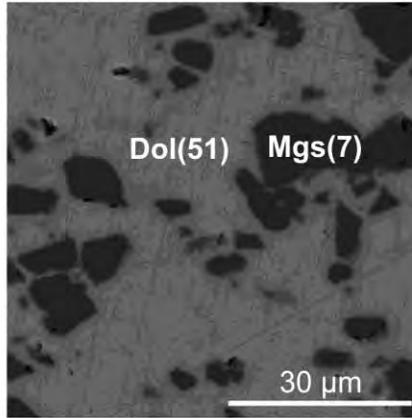
c. D071; 70; 1175 °C; 1 h.
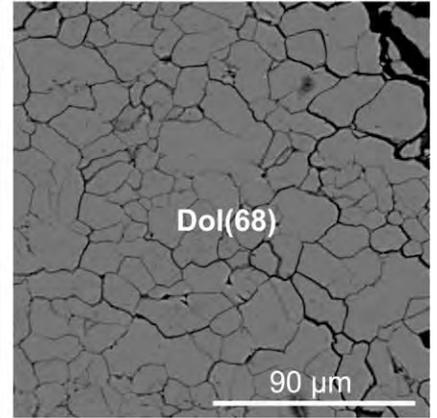
d. D071; 40; 1175 °C; 1 h.
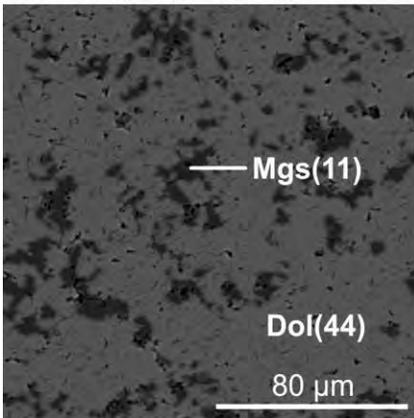
e. D072; 70; 1250 °C; 1 h.
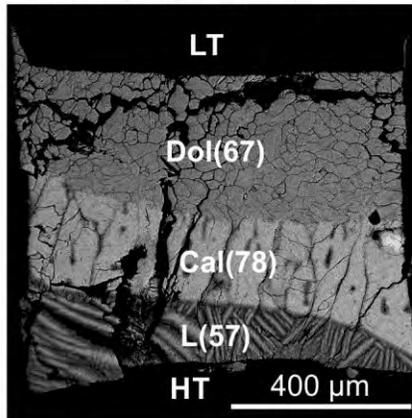
f. D072; 57; 1250 °C; 1 h.
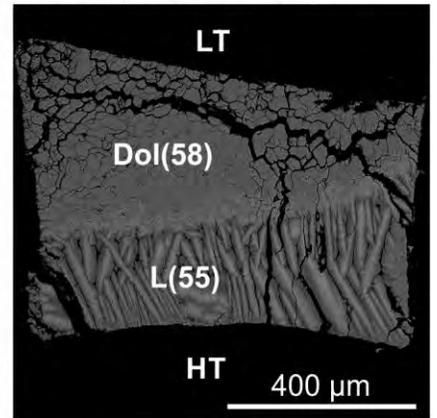
g. D072; 40; 1250 °C; 1 h.
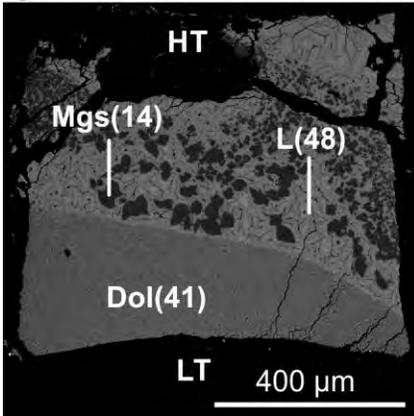
h. D053; 70; 1300 °C; 1 h.
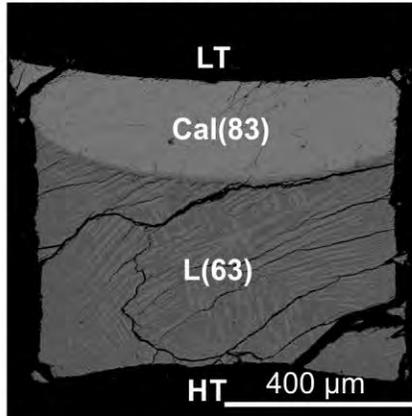
i. D053; 50; 1300 °C; 1 h.

368

14
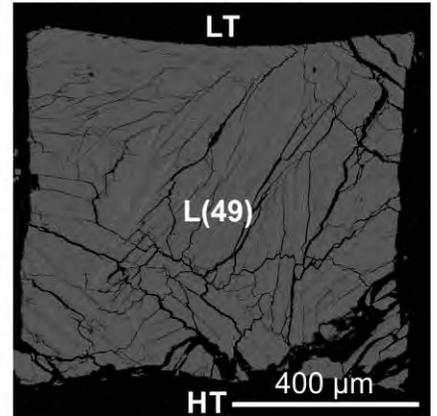
Run No.; $X(CaCO_3)$, mol%; temperature; run duration
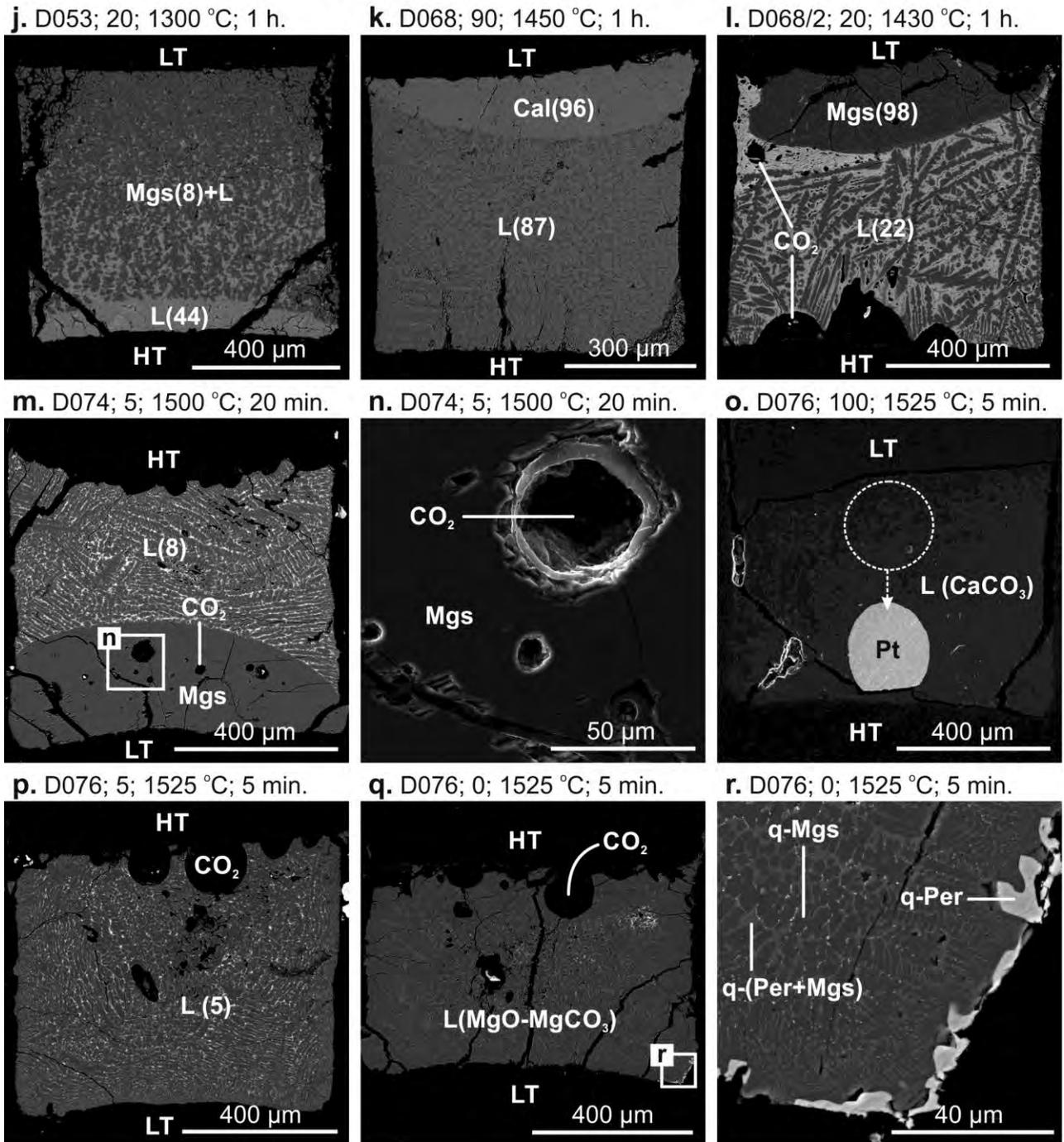
Fig. 4. BSE (a-m, p-r) and SEM (n-o) images of sample cross-sections illustrating phase relations in the system $CaCO_3$-$MgCO_3$ at 3 GPa and 1000-1525 °C. The numbers in parentheses indicate Ca# of carbonate phases. HT – high-temperature side. LT – low-temperature side. Gravity vector is directed downwards.
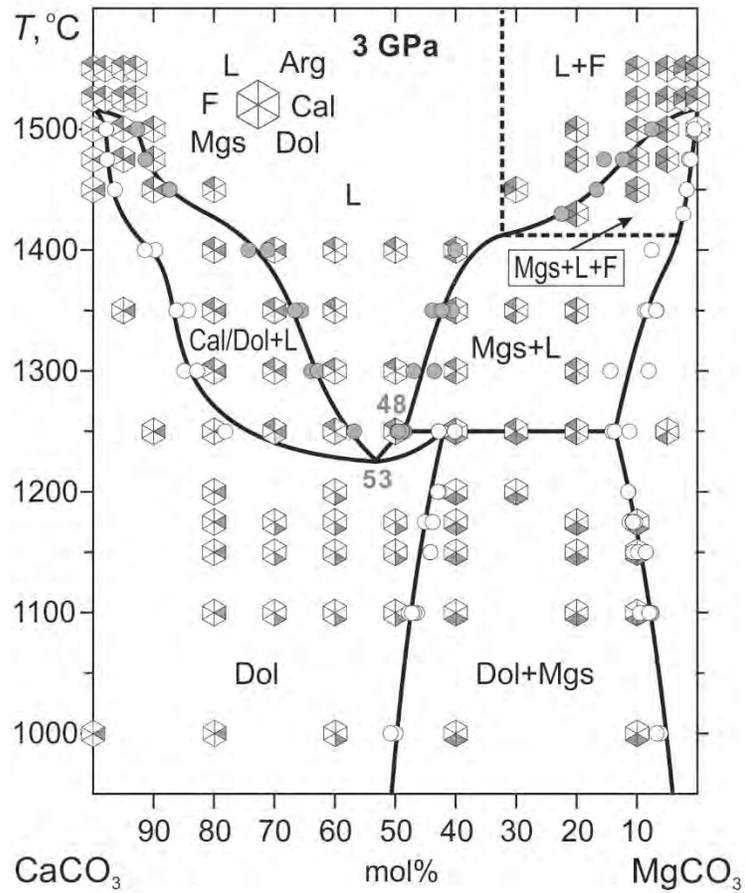
15

Fig. 5. Isobaric *T-X* diagram for the system $CaCO_3$-$MgCO_3$ at 3 GPa. Cal or Ca-Dol – Mg-bearing calcite or Ca-rich dolomite, Dol – dolomite, Mgs – magnesite, F – CO_2 fluid, L – liquid. Open and grey circles indicate composition of solid phases and liquid measured by EDS. Grey numbers denote eutectic and peritectic compositions in mol% $CaCO_3$.

374
375
376
377
378
379
380
381

16

Run No.; $X(CaCO_3)$, mol%; temperature; run duration

a. D026; 80; 1050 °C; 96 h.   **b.** D026; 60; 1050 °C; 96 h.   **c.** D026; 40; 1050 °C; 96 h.

d. D031; 90; 1150 °C; 53 h.   **e.** D031; 90; 1150 °C; 53 h.   **f.** D123; 99; 1300 °C; 62 h.

g. D010; 60; 1400 °C; 24 h.   **h.** D010; 20; 1400 °C; 24 h.   **i.** D010; 20; 1400 °C; 24 h.

j. D030; 80; 1450 °C; 7 h.   **k.** D030; 70; 1450 °C; 7 h.   **l.** D030; 50; 1450 °C; 7 h.


382

17
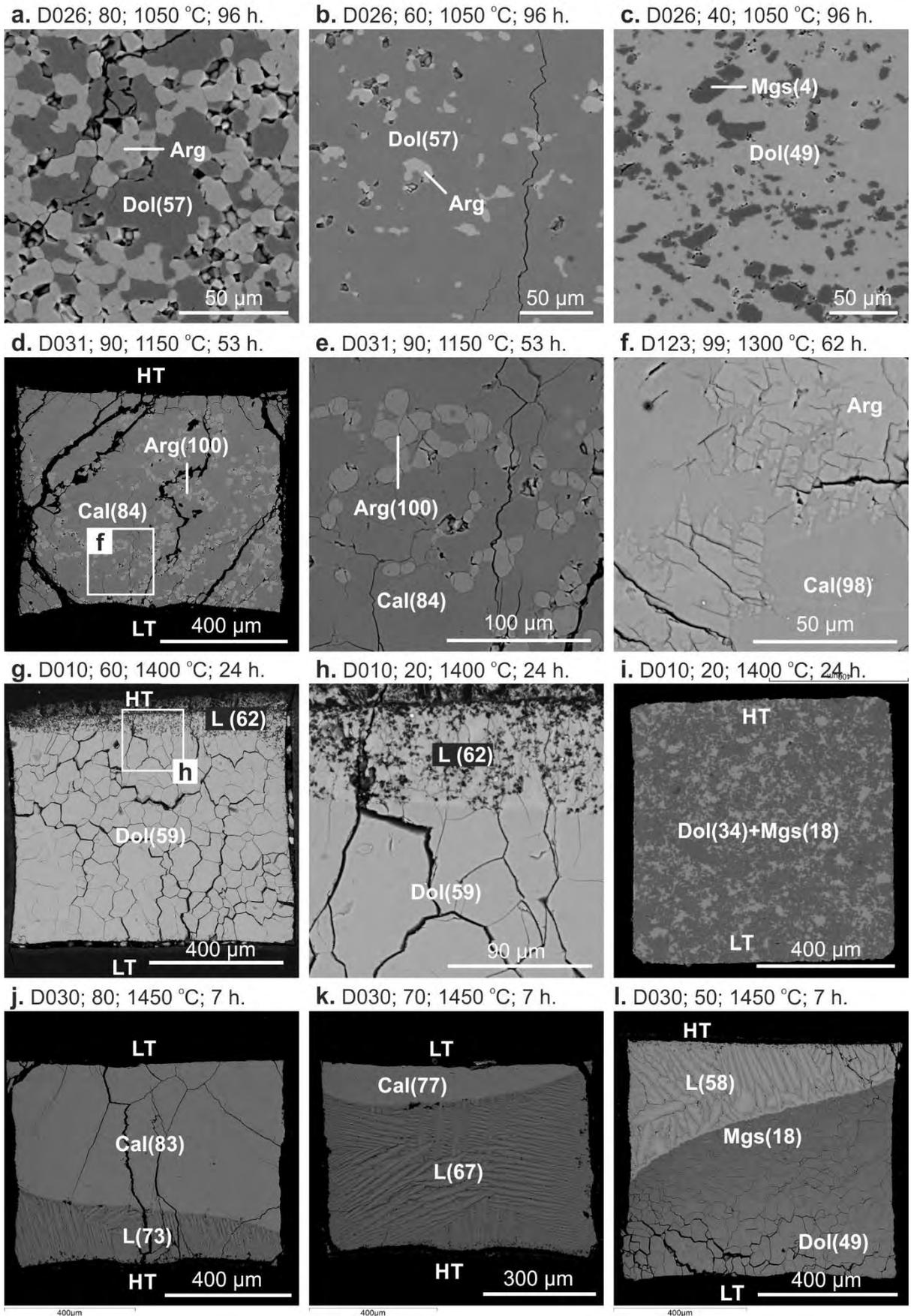
Run No.; $X(CaCO_3)$, mol%; temperature; run duration
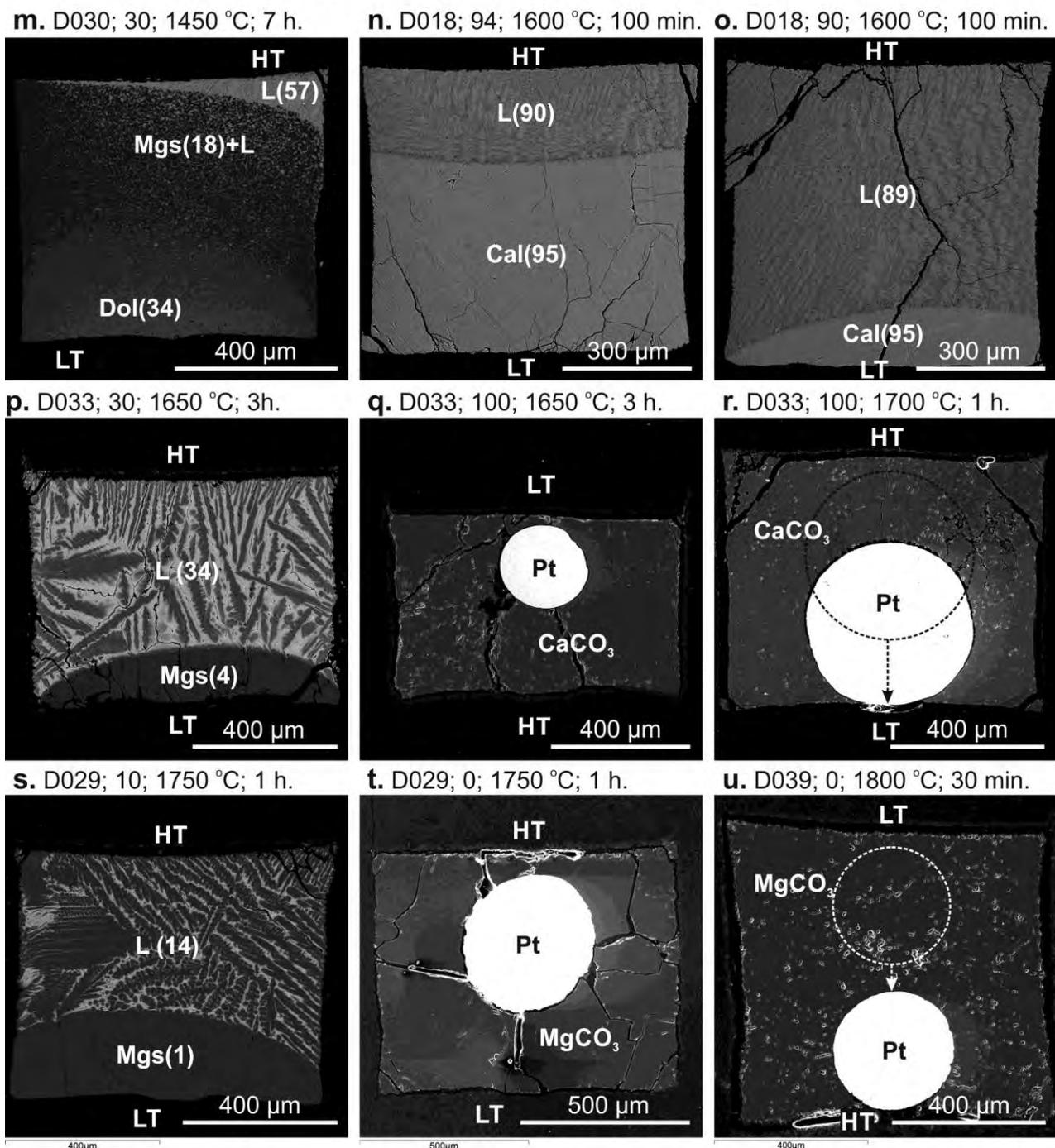
Fig. 6. BSE (a-p, s) and SEM (q, r, t, u) images illustrating phase relations in the system $CaCO_3$-$MgCO_3$ at 6 GPa. The numbers in parentheses indicate Ca# of corresponding carbonate phases. HT – high-temperature side. LT – low-temperature side. Gravity vector is directed downwards.

18
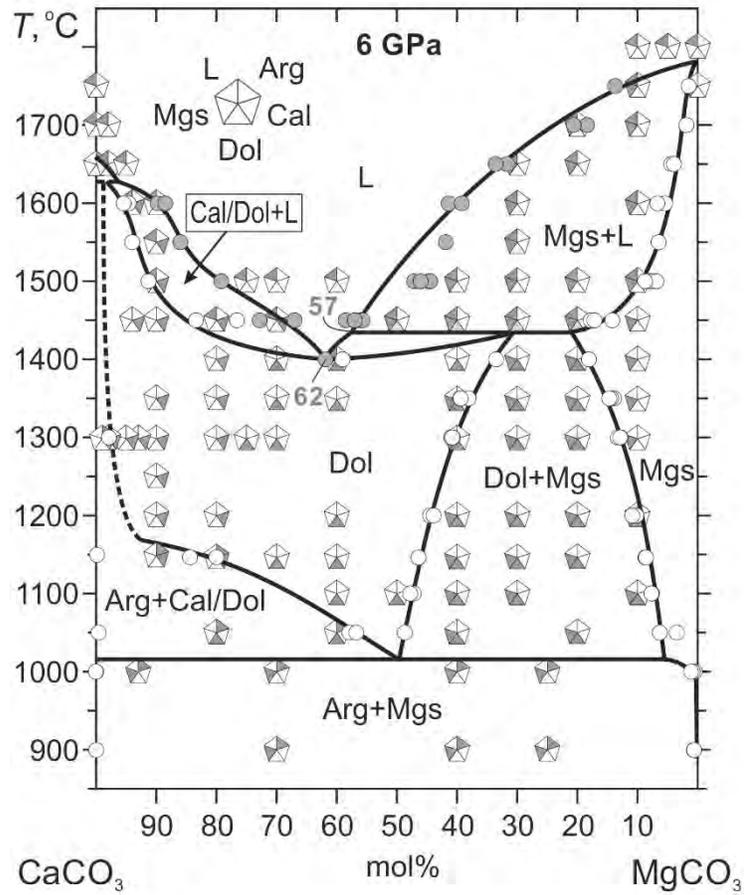
387

388   Fig. 7. Isobaric *T-X* diagram for the system CaCO₃-MgCO₃ at 6 GPa. Arg – aragonite, Cal – calcite,

389   Dol – dolomite, Mgs – magnesite, L – liquid. Open and grey circles indicate composition of solid

390   phases and liquid measured by EDS. Grey numbers denote eutectic and peritectic compositions in

391   mol% CaCO₃.

392
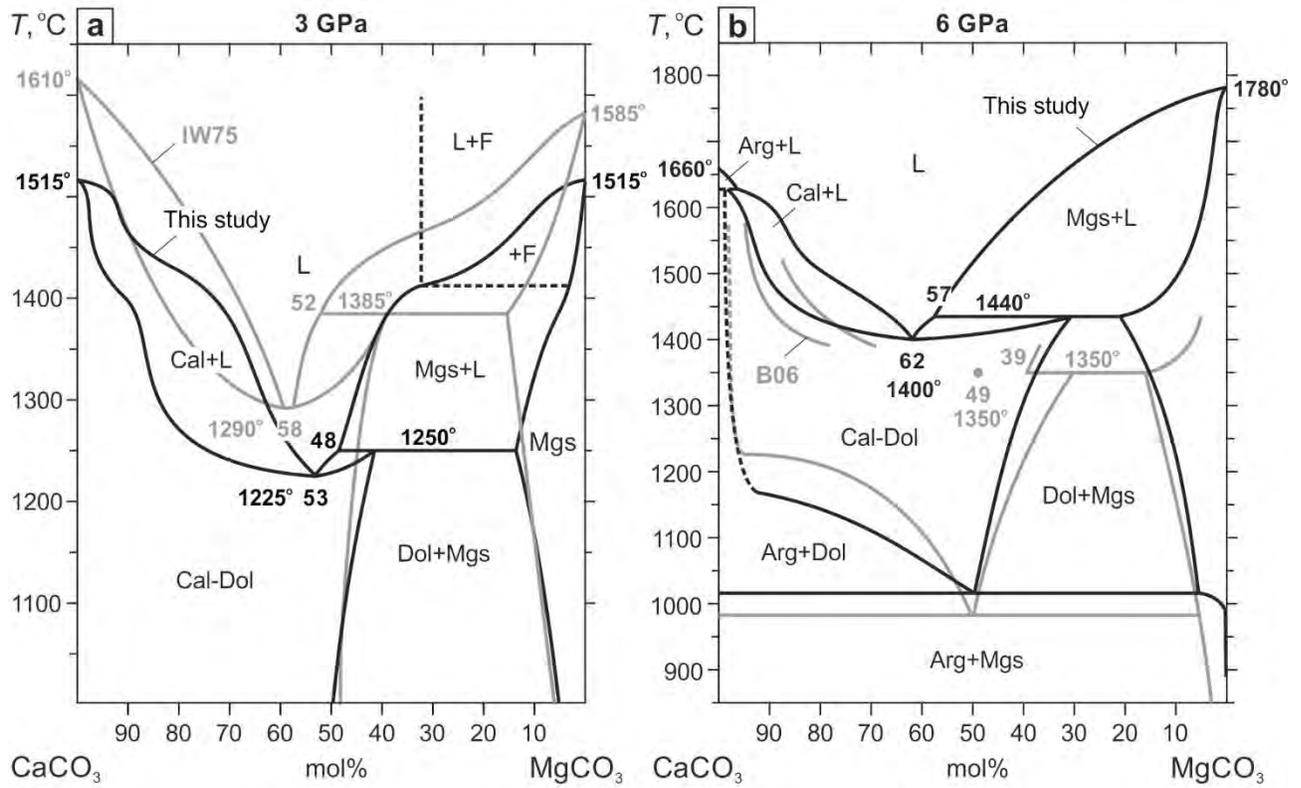
393

394 Fig. 8. Comparison of *T-X* phase diagrams for the CaCO₃-MgCO₃ system at 3 and 6 GPa determined
395 by this and previous studies. IW75 – (Irving and Wyllie, 1975); B06 – (Buob et al., 2006).

396

397
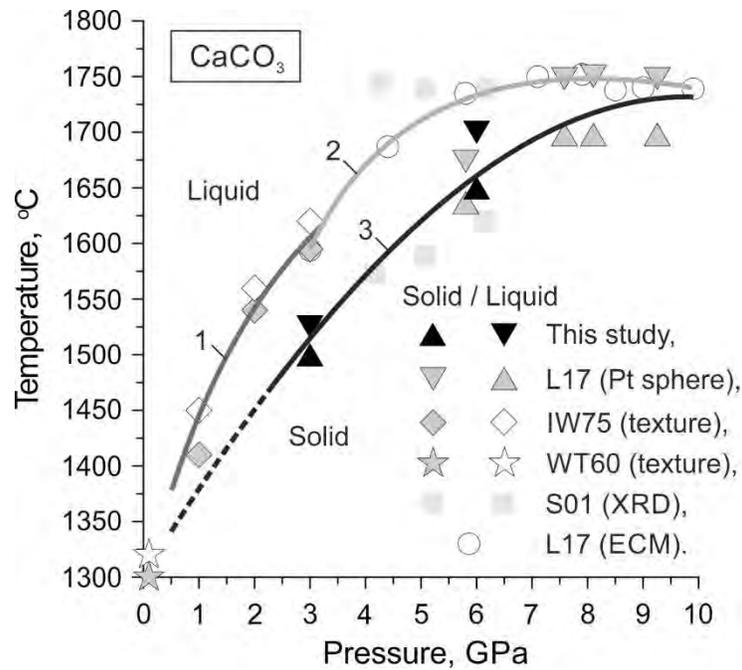
398

399   Fig. 9. Melting curve of $CaCO_3$. 1 – melting curve based on quenched experiments (Irving and
400   Wyllie, 1975) with duration of 2 min at 2-3 GPa and 4-5 min at 1 GPa. Identification of melt based
401   on textural criteria. 2 – melting curve obtained using electrical conductivity measurements (ECM)
402   (Li et al., 2017). 3 – melting curve based on falling sphere experiments in this study and in (Li et al.,
403   2017). WT60 – incongruent melting Cal = L + F (Wyllie and Tuttle, 1960); IW75 – (Irving and
404   Wyllie, 1975); S01 – (Suito et al., 2001); L17 – (Li et al., 2017).

405

406

407
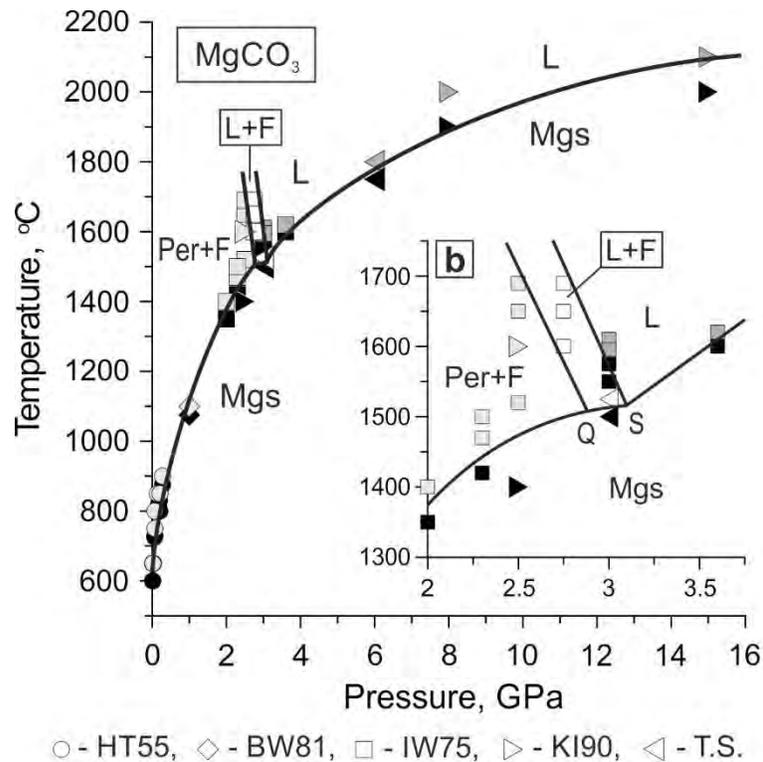
Fig. 10. Experimentally-determined phase relations for $MgCO_3$. Mgs – magnesite, Per – periclase, F – CO_2 fluid, L – liquid, Q – invariant point, S – singular point. Filled symbols denote runs with Mgs. Dark grey symbols denote runs with molten $MgCO_3$. Light grey symbols denote runs with the Per + F ± Mgs assemblage. Open symbols denote runs where MgO-bearing $MgCO_3$ liquid coexists with CO_2 fluid. HT55 – (Harker and Tuttle, 1955), BW81 – (Byrnes and Wyllie, 1981), IW75 – (Irving and Wyllie, 1975), KI90 – (Katsura and Ito, 1990), T.S. – this study.

414

22

415
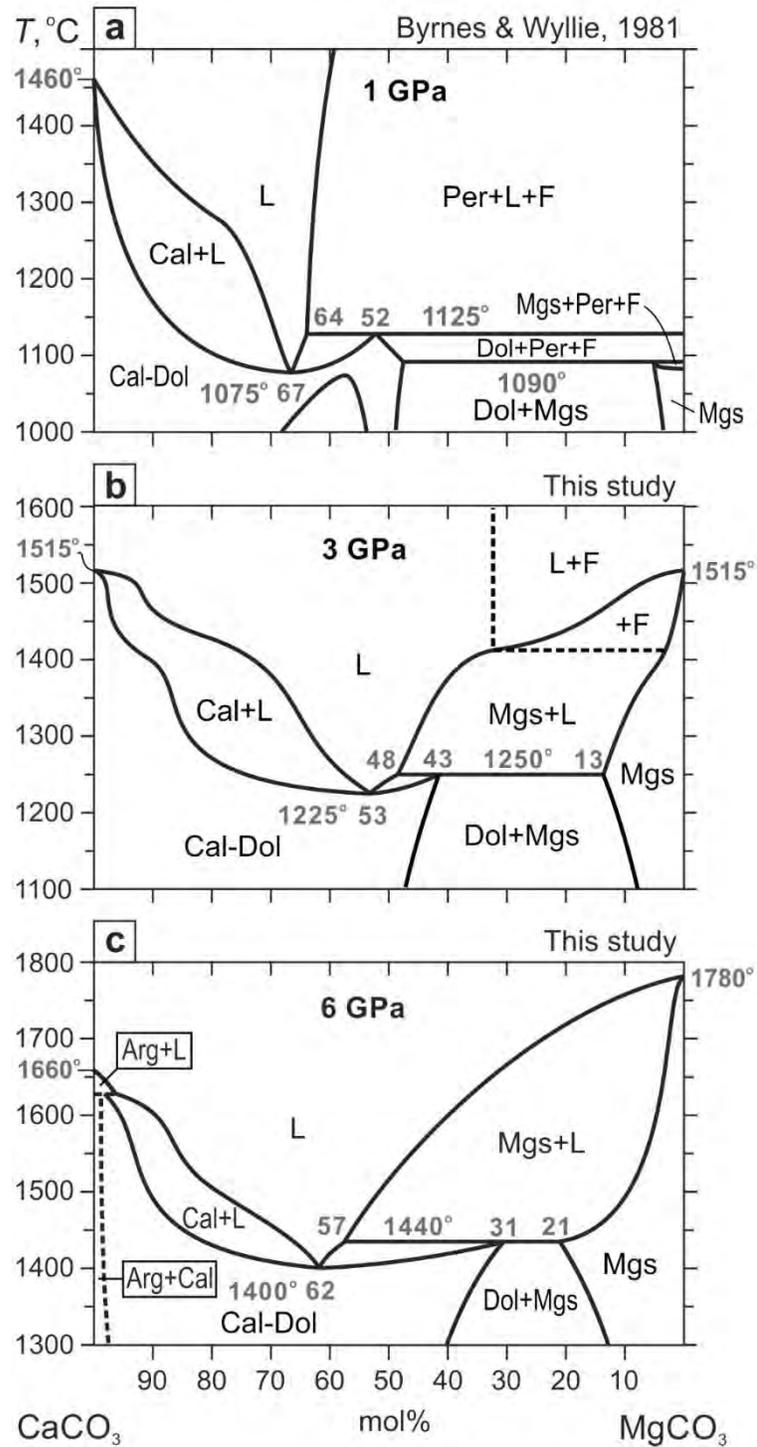
Fig. 11. *T-X* phase diagrams for the $CaCO_3$-$MgCO_3$ join at (a) 1 GPa Byrnes and Wyllie (1981); (b) 3 GPa this study; (c) 6 GPa this study. Grey numbers denote eutectic and peritectic compositions in mol% $CaCO_3$ and melting temperatures of end-members.

419

23
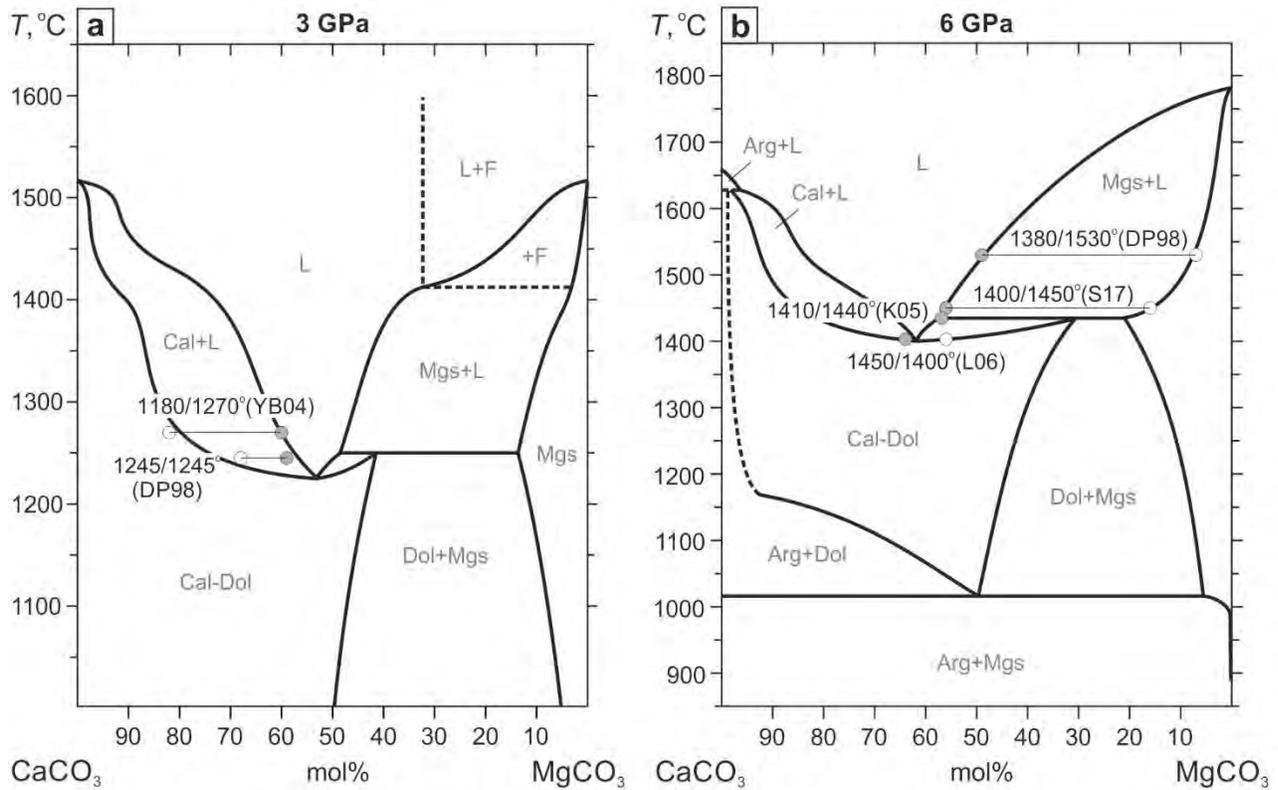
Fig. 12. Comparison of phase relations in the system $CaCO_3$–$MgCO_3$ at 3 GPa (a) and 6 GPa (b) with the projected compositions of carbonate minerals (open circles) and melts (grey circles) from near-solidus experiments in the carbonate-silicate systems. DP98 – CMAS-CO_2 peridotite (Dalton and Presnall, 1998); YB04 – eclogite (Yaxley and Brey, 2004); K05 – CMAS-CO_2 (Keshav et al., 2005); L06 – $CaCO_3$+MgO+2SiO_2 system (Luth, 2006); S17 – $CaMgSi_2O_6$+2$MgCO_3$ system (Shatskiy et al., 2017).

References

Akella, J., and Kennedy, G.C. (1971) Melting of gold, silver, and copper - Proposal for a new high-pressure calibration scale. Journal of Physical Research, 76, 4969-4977.

Amundsen, H.E. (1987) Evidence for liquid immiscibility in the upper mantle. Nature, 327, 692-695.

Bulanova, G.P., and Pavlova, L.P. (1987) Magnesite peridotite assemblage in diamond from the Mir pipe. Doklady Akademii Nauk SSSR, 295, 1452-1456.

Buob, A. (2003) The system $CaCO_3$-$MgCO_3$: Experiments and thermodinamic solid solutions at high pressure and temperature, Doctor of natural science, p. 109. Swiss Federal Institute of Technology, Zürich.

Buob, A., Luth, R.W., Schmidt, M.W., and Ulmer, P. (2006) Experiments on $CaCO_3$-$MgCO_3$ solid solutions at high pressure and temperature. American Mineralogist, 91, 435-440.

Byrnes, A.P., and Wyllie, P.J. (1981) Subsolidus and melting relations for the join $CaCO_3$-$MgCO_3$ at 10 kbar. Geochimica Et Cosmochimica Acta, 45, 321-328.

443   Dalton, J.A., and Presnall, D.C. (1998) Carbonatitic melts along the solidus of model lherzolite in
444   the system CaO-MgO-Al$_2$O$_3$-SiO$_2$-CO$_2$ from 3 to 7 GPa. Contributions to Mineralogy and
445   Petrology, 131, 123-135.
446   Dasgupta, R., Hirschmann, M.M., and Withers, A.C. (2004) Deep global cycling of carbon
447   constrained by the solidus of anhydrous, carbonated eclogite under upper mantle conditions.
448   Earth and Planetary Science Letters, 227, 73-85.
449   Dasgupta, R., and Hirschmann, M.M. (2007) Effect of variable carbonate concentration on the
450   solidus of mantle peridotite. American Mineralogist, 92, 370-379.
451   Decker, D.L., Bassett, W.A., Merrill, L., Hall, H.T., and Barnett, J.D. (1972) High-pressure
452   calibration a critical review. J. Phys. Chem. Ref. Data. , 1, 1-79.
453   Dobrzhinetskaya, L.F., Wirth, R., and Green, H.W. (2006) Nanometric inclusions of carbonates in
454   Kokchetav diamonds from Kazakhstan: A new constraint for the depth of metamorphic
455   diamond crystallization. Earth and Planetary Science Letters, 243, 85-93.
456   Eggler, D.H. (1978) The effect of CO$_2$ upon partial melting of peridotite in the system Na$_2$O-CaO-
457   Al$_2$O$_3$-MgO-SiO$_2$-CO$_2$ to 35 kb with an analysis of melting in a peridotite-H$_2$O-CO$_2$ system.
458   American Journal of Science, 278, 305-343.
459   Grassi, D., and Schmidt, M.W. (2011) The melting of carbonated pelites from 70 to 700 km depth.
460   Journal of Petrology, 52, 765-789.
461   Haines, P. (2002) Principles of thermal analysis and calorimetry. 216 p. Royal society of chemistry.
462   Harker, R.I., and Tuttle, O.F. (1955) Studies in the system CaO-MgO-CO$_2$; Part 1, The thermal
463   dissociation of calcite, dolomite and magnesite. American Journal of Science, 253, 209-224.
464   Hemingway, B.S., Bohlen, S.R., Hankins, W., Westrum, E.F., and Kuskov, O.L. (1998) Heat
465   capacity and thermodynamic properties for coesite and jadeite, reexamination of the quartz-
466   coesite equilibrium boundary. American Mineralogist, 83, 409-418.
467   Huang, W.L., and Wyllie, P.J. (1976) Melting relationships in the systems CaO-CO$_2$ and MgO-CO$_2$
468   to 33 kilobars. Geochimica Et Cosmochimica Acta, 40, 129-132.
469   Ionov, D.A., Dupuy, C., O'Reilly, S.Y., Kopylova, M.G., and Genshaft, Y.S. (1993) Carbonated
470   peridotite xenoliths from Spitsbergen: implications for trace element signature of mantle
471   carbonate metasomatism. Earth and Planetary Science Letters, 119, 283-297.
472   Ionov, D.A., O'Reilly, S.Y., Genshaft, Y.S., and Kopylova, M.G. (1996) Carbonate-bearing mantle
473   peridotite xenoliths from Spitsbergen: phase relationships, mineral compositions and trace-
474   element residence. Contributions to Mineralogy and Petrology, 125, 375-392.
475   Irving, A.J., and Wyllie, P.J. (1975) Subsolidus and melting relationships for calcite, magnesite and
476   the join CaCO$_3$-MgCO$_3$ to 36 kb. Geochimica et Cosmochimica Acta, 39, 35-53.
477   Katsura, T., and Ito, E. (1990) Melting and subsolidus relations in the MgSiO$_3$–MgCO$_3$ system at
478   high pressures: implications to evolution of the Earth's atmosphere. Earth and Planetary
479   Science Letters, 99, 110–117.
480   Kerrick, D.M., and Connolly, J.A.D. (2001a) Metamorphic devolatilization of subducted oceanic
481   metabasalts: implications for seismicity, arc magmatism and volatile recycling. Earth and
482   Planetary Science Letters, 189, 19-29.
483   -. (2001b) Metamorphic devolatilization of subducted marine sediments and the transport of
484   volatiles into the Earth's mantle. Nature, 411, 293-296.
485   Keshav, S., Corgne, A., Gudfinnsson, G.H., Bizimis, M., McDonough, W.F., and Fei, Y. (2005)
486   Kimberlite petrogenesis: insights from clinopyroxene-melt partitioning experiments at 6 GPa
487   in the CaO-MgO-Al$_2$O$_3$-SiO$_2$-CO$_2$ system. Geochimica et Cosmochimica Acta, 69, 2829-
488   2845.

489   Kiseeva, E.S., Litasov, K.D., Yaxley, G.M., Ohtani, E., and Kamenetsky, V.S. (2013) Melting phase
490   relations of carbonated eclogite at 9-21 GPa and alkali-rich melts in the deep mantle. Journal
491   of Petrology, DOI: 10.1093/petrology/egt023.

492   Kogarko, L., Henderson, C.M., and Pacheco, H. (1995) Primary Ca-rich carbonatite magma and
493   carbonate-silicate-sulphide liquid immiscibility in the upper mantle. Contributions to
494   Mineralogy and Petrology, 121, 267-274.

495   Korsakov, A.V., and Hermann, J. (2006) Silicate and carbonate melt inclusions associated with
496   diamonds in deeply subducted carbonate rocks. Earth and Planetary Science Letters, 241,
497   104-118.

498   Korsakov, A.V., De Gussem, K., Zhukov, V.P., Perraki, M., Vandenabeele, P., and Golovin, A.V.
499   (2009) Aragonite-calcite-dolomite relationships in UHPM polycrystalline carbonate
500   inclusions from the Kokchetav Massif, northern Kazakhstan. European Journal of
501   Mineralogy, 21, 1301-1311.

502   Lavrent'ev, Y.G., Karmanov, N., and Usova, L. (2015) Electron probe microanalysis of minerals:
503   Microanalyzer or scanning electron microscope? Russian Geology and Geophysics, 56,
504   1154-1161.

505   Li, Z., Li, J., Lange, R., Liu, J., and Militzer, B. (2017) Determination of calcium carbonate and
506   sodium carbonate melting curves up to Earth's transition zone pressures with implications for
507   the deep carbon cycle. Earth and Planetary Science Letters, 457, 395-402.

508   Litasov, K.D., and Ohtani, E. (2009) Solidus and phase relations of carbonated peridotite in the
509   system $CaO-Al_2O_3-MgO-SiO_2-Na_2O-CO_2$ to the lower mantle depths. Physics of the Earth
510   and Planetary Interiors, 177, 46-58.

511   Litasov, K.D., and Ohtani, E. (2010) The solidus of carbonated eclogite in the system $CaO-Al_2O_3-$
512        $MgO-SiO_2-Na_2O-CO_2$ to 32 GPa and carbonatite liquid in the deep mantle. Earth and
513   Planetary Science Letters, 295, 115-126.

514   Luth, R.W. (2006) Experimental study of the $CaMgSi_2O_6-CO_2$ system at 3-8 GPa. Contributions to
515   Mineralogy and Petrology, 151, 141-157.

516   Meyer, H.O.A., and McCallum, M.E. (1986) Mineral inclusions in diamonds from the Sloan
517   kimberlites, Colorado. Journal of Geology, 94, 600-612.

518   Murakami, T., Wallis, S., Enami, M., and Kagi, H. (2008) Forearc diamond from Japan. Geology,
519   36, 219-222.

520   Ono, S., Kikegawa, T., and Higo, Y. (2011) In situ observation of a garnet/perovskite transition in
521        $CaGeO_3$. Physics and Chemistry of Minerals, 38, 735-740.

522   Phillips, D., and Harris, J.W. (1995) Geothermobarometry of diamond inclusions from the De Beers
523   pool mines, Kimberley, South Africa. VI Int. Kimberlite Conf.: Extended Abstr., p. 441-442,
524   Novosibirsk, Russia.

525   Shatskiy, A., Katsura, T., Litasov, K.D., Shcherbakova, A.V., Borzdov, Y.M., Yamazaki, D.,
526   Yoneda, A., Ohtani, E., and Ito, E. (2011) High pressure generation using scaled-up Kawai-
527   cell. Physics of the Earth and Planetary Interiors, 189, 92-108.

528   Shatskiy, A., Sharygin, I.S., Gavryushkin, P.N., Litasov, K.D., Borzdov, Y.M., Shcherbakova, A.V.,
529   Higo, Y., Funakoshi, K., Palyanov, Y.N., and Ohtani, E. (2013) The system $K_2CO_3-MgCO_3$
530   at 6 GPa and 900-1450 ºC. American Mineralogist, 98, 1593-1603.

531   Shatskiy, A., Gavryushkin, P.N., Litasov, K.D., Koroleva, O.N., Kupriyanov, I.N., Borzdov, Y.M.,
532   Sharygin, I.S., Funakoshi, K., Palyanov, Y.N., and Ohtani, E. (2015) Na-Ca carbonates
533   synthesized under upper-mantle conditions: Raman spectroscopic and X-ray diffraction
534   studies. European Journal of Mineralogy, 27, 175-184.

535   Shatskiy, A., Podborodnikov, I.V., Arefiev, A.V., Litasov, K.D., Chanyshev, A.D., Sharygin, I.S.,
536   Karmanov, N.S., and Ohtani, E. (2017) Effect of alkalis on the reaction of clinopyroxene

26

537   with Mg-carbonate at 6 GPa: Implications for partial melting of carbonated lherzolite.
538   American Mineralogist, 102, 1934-1946.
539 Shatsky, V., Ragozin, A., Zedgenizov, D., and Mityukhin, S. (2008) Evidence for multistage
540   evolution in a xenolith of diamond-bearing eclogite from the Udachnaya kimberlite pipe.
541   Lithos, 105, 289-300.
542 Shatsky, V.S., Sobolev, N.V., and Vavilov, M.A. (1995) Diamond-bearing metamorphic rocks from
543   the Kokchetav massif (Northern Kazakhstan). In R.G. Coleman, and X. Wang, Eds.
544   Ultrahigh Pressure Metamorphism, p. 427-455. Cambridge University Press.
545 Sobolev, N.V., and Shatsky, V.S. (1990) Diamond inclusions in garnets from metamorphic rocks: a
546   new environment for diamond formation. Nature, 343, 742-746.
547 Sobolev, N.V., Kaminsky, F.V., Griffin, W.L., Yefimova, E.S., Win, T.T., Ryan, C.G., and
548   Botkunov, A.I. (1997) Mineral inclusions in diamonds from the Sputnik kimberlite pipe,
549   Yakutia. Lithos, 39, 135-157.
550 Stachel, T., Harris, J.W., and Brey, G.P. (1998) Rare and unusual mineral inclusions in diamonds
551   from Mwadui, Tanzania. Contributions to Mineralogy and Petrology, 132, 34-47.
552 Suito, K., Namba, J., Horikawa, T., Taniguchi, Y., Sakurai, N., Kobayashi, M., Onodera, A.,
553   Shimomura, O., and Kikegawa, T. (2001) Phase relations of $CaCO_3$ at high pressure and
554   high temperature. American Mineralogist, 86, 997-1002.
555 Thomsen, T.B., and Schmidt, M.W. (2008) Melting of carbonated pelites at 2.5–5.0 GPa, silicate–
556   carbonatite liquid immiscibility, and potassium–carbon metasomatism of the mantle. Earth
557   and Planetary Science Letters, 267, 17-31.
558 Thomson, A.R., Walter, M.J., Kohn, S.C., and Brooker, R.A. (2016) Slab melting as a barrier to
559   deep carbon subduction. Nature, 529, 76-79.
560 Wallace, M.E., and Green, D.H. (1988) An experimental determination of primary carbonatite
561   magma composition. Nature, 335, 343-346.
562 Wang, A., Pasteris, J.D., Meyer, H.O.A., and DeleDuboi, M.L. (1996) Magnesite-bearing inclusion
563   assemblage in natural diamond. Earth and Planetary Science Letters, 141, 293-306.
564 Wyllie, P.J., and Tuttle, O.F. (1960) The system $CaO–CO_2–H_2O$ and the origin of carbonatites.
565   Journal of Petrology, 1, 1-46.
566 Wyllie, P.J., and Huang, W. (1975) Peridotite, kimberlite, and carbonatite explained in the system
567          $CaO-MgO-SiO_2-CO_2$. Geology, 3, 621-624.
568 Wyllie, P.J., and Huang, W.-L. (1976) Carbonation and melting reactions in the system $CaO–MgO–$
569          $SiO_2–CO_2$ at mantle pressures with geophysical and petrological applications. Contributions
570   to Mineralogy and Petrology, 54, 79-107.
571 Yaxley, G.M., and Brey, G.P. (2004) Phase relations of carbonate-bearing eclogite assemblages
572   from 2.5 to 5.5 GPa: implications for petrogenesis of carbonatites. Contributions to
573   Mineralogy and Petrology, 146, 606-619.
574 Zedgenizov, D.A., Shatskiy, A., Ragozin, A.L., Kagi, H., and Shatsky, V.S. (2014) Merwinite in
575   diamond from São Luis, Brazil: A new mineral of the Ca-rich mantle environment.
576   American Mineralogist, 99, 547-550.

577